Solar Energy Materials & Solar Cells 246 (2022) 111922

Contents lists available at ScienceDirect

Solar Energy Materials and Solar Cells

journal homepage: www.elsevier.com/locate/solmat

Photo-thermo-electric modeling of photon-enhanced thermionic emission with concentrated solar power

Hao Qiu, Haoran Xu [*], Mingjiang Ni, Gang Xiao [**]

State Key Laboratory of Clean Energy Utilization, Zhejiang University, 38 Zheda Road, Hangzhou, 310027, China

ARTICLE INFO

Keywords:
Photon-enhanced thermionic emission
Concentrated solar power
Photo-thermo-electric analysis
Space-charge effect
Full spectrum utilization

ABSTRACT

Photon-enhanced thermionic emission (PETE) is an advanced technology that combines both the photoelectric and the thermionic effects synergistically into a single device for direct electricity generation. However, its industrial-level application is still missing partly due to the lack of advanced models to analyze its operating characteristics and to understand the synergistic mechanism. Herein, we develop a numerical model of PETE by fully considering the optical, the electrical and the thermodynamic aspects with one-dimensional steady-state continuity equations of carriers in the semiconductor cathode. A hybrid PETE-Stirling cycle system is also proposed to yield an output power density of 162.65 kW/m^2 with 32.8% conversion efficiency. The PETE conversion efficiency keeps ~20% with the optimal electron affinity increases from 0.5 to 1.14 eV as solar concentration ratio varies from 100 to 500. The cathode thickness should be optimized by considering both solar absorption and photon enhancement, where the thickness range of 0.78–1.52 μm is obtained for 50–500 suns. The inter-electrode gap is also found to significantly affect the PETE performance by regulating both the space-charge effect and near-field radiation, where the range of 0.5–2 μm is recommended. This work can serve as a foundation to understand the working mechanism of PETE converters and provide guidelines for the performance evaluation.

1. Introduction

Solar energy is clean, abundant and sustainable energy, and conventionally harvested via the photovoltaic (PV) and the solar thermal (ST) technologies. To realize its full spectrum utilization, new technologies are being developed, such as the concentrated spectral-splitting, the hybrid photovoltaic-thermal utilization [1], and the concentrated photochemical-photovoltaic-thermochemical (CP-PV-T) [2]. A thermionic emission converter (TEC) can be applied for ST power generation, which consists of a metal cathode and an anode arranged parallel in a vacuum house [3]. TEC has made great progress toward high power output. Some novel electrode materials were proposed such as carbon nanotube emitters, textured/diamond/graphene-based electrodes, and plasmonic thermionic converters. To synergistically utilize the electrons and photons emitted by the cathode, Datas et al. [4,5] proposed hybrid thermionic-photovoltaic converters (TIPV), in which a photovoltaic cell was applied to enhance electricity generation. Recently, the TIPV prototypes were developed and measured, and the experimental results demonstrated significant potential of TIPV converters [6,7]. In addition, solar thermionic-thermoelectric generator was proposed to use the waste heat of TEC for additional power generation by thermoelectric technology [8,9]. The photon-enhanced thermionic emission (PETE) is especially suitable for concentrated solar power applications, as it combines the photoelectric and the thermionic effects into a single device to realize a full spectrum harvesting and avoids spectral-splitting [10]. A PETE converter can gain a theoretical conversion efficiency of >50% when thermally in tandem with a secondary heat engine [11].

A PETE converter has a configuration similar with a TEC converter, but uses a semiconductor instead of metallic materials as the cathode. As shown in Fig. 1, incident solar photons with energy over the bandgap (E_g) of the cathode semiconductor, i.e., over-bandgap photons, can excite electrons from the valence-band (E_V) to the conduction-band (E_C). The photoexcited electrons will diffuse to the emitting surface while absorbing heat to reach a higher kinetic energy. The electrons that overcome the electron affinity (χ) can emit directly to the anode and return to the cathode through the outer circuit to generate electric current. However, Rahman et al. [12] recently pointed out that the so-called semiconductor thermionic energy converter exhibits

* Corresponding author.
** Corresponding author.
E-mail addresses: haoranxu@zju.edu.cn (H. Xu), xiaogangtianmen@zju.edu.cn (G. Xiao).

https://doi.org/10.1016/j.solmat.2022.111922
Received 28 March 2022; Received in revised form 18 June 2022; Accepted 19 July 2022
Available online 8 August 2022

Nomenclature

A	Richardson constant, A/(m^2·K^2)
C	solar concentration ratio
D_n (D_p)	electron (hole) diffusion coefficient, m^2/s
E_A	impurity energy level, eV
E_C	the conduction band minimum, eV
E_V	the valence band maximum, eV
E_F	Fermi level, eV
E_g	bandgap of the cathode, eV
ΔE_a (ΔE_c)	motive barrier of the anode (cathode), eV
G	photogeneration rate of electron-hole, 1/(m^3·s)
J	current density, A/m^2
N_A	semiconductor doping density, 1/m^3
N_C	the effective density of states in the conduction band, 1/m^3
N_V	the effective density of states in the valence band, 1/m^3
N_a (N_c)	electron density emitted by the anode (cathode), 1/m^2
P_{PETE}	output power density of PETE converter, W/m^2
P_{SE}	output power of Stirling engine, W
Q_{sun}	incident solar energy, W/m^2
$Q_{electron}$	heat transferred by emitted electrons, W/m^2
$Q_{rad,\ C\_amb}$	radiative heat loss from the cathode to the ambient, W/m^2
Q_{rad,C_A}	radiative heat loss between the two electrodes, W/m^2
$Q_{rad,\ recom}$	radiative energy of emitted blackbody photons above the bandgap, W/m^2
$Q_{penetrate}$	solar energy penetrating through the cathode, W/m^2
Q_{lead}	heat loss in the lead, W/m^2
Q_{anode}	waste heat from the anode, W/m^2
Q_{SE}	the required heating power of the Stirling engine, W
R_{rad}	radiative recombination rate, 1/(m^3·s)
R_{Auger}	Auger recombination rate, 1/(m^3·s)
R_{SRH}	SRH recombination rate, 1/(m^3·s)
R_{lead}	lead resistance, Ω
S	working area of the PETE converter, m^2
$S_{n,0}$ ($S_{n,t}$)	surface recombination rate on photon incident surface (electron emission surface)
T_a	the anode temperature, K
T_c	the cathode temperature, K
T_0	the ambient temperature, K
V	output voltage, V
V_s	saturation voltage, V
V_{MPP}	voltage at the maximum power point, V
c	speed of light, m/s
d	interelectrode gap size, m
e	elementary charge, C
h	Planck's constant, J·s
k	Boltzmann's constant, J/K
m^*_n	electron effective mass at the conduction band minimum, kg
m^*_p	hole effective mass at the valence band maximum, kg
n	conduction-band electron concentration, 1/m^3
n_{eq}	equilibrium conduction-band electron concentration, 1/m^3
p	valence-band hole concentration, 1/m^3
p_{eq}	equilibrium valence-band hole concentration, 1/m^3
Δn (Δp)	non-equilibrium electron (hole) concentration, 1/m^3
t	cathode thickness, m

Greek symbols

α	photon absorption coefficient, 1/m^3
λ	photon wavelength, m
λ_0	cut-off wavelength, m
μ	carrier mobility, m^2/(V·s)
ν	photon frequency, 1/s
τ_{SRH}	carrier SRH lifetimes, s
ϕ_c	cathode work function, eV
ϕ_a	anode work function, eV
ψ_m	the maximum motive barrier, eV
η	conversion efficiency of the hybrid system
η_{PETE}	conversion efficiency of the PETE converter
$\eta_{anode\text{-}SE}$	heat transfer efficiency of PETE waste heat

Subscripts

n	electron
p	hole

photon-enhancement mode only under certain conditions, otherwise it performs pure thermionic emission mode. Therefore, PETE converters deserve further detailed study and design.

Several PETE models have been built, including models ignoring the carrier distribution in semiconductors (0-D models) and models considering one-dimensional distribution of carriers (1-D models). To evaluate the efficiency limit of the PETE converter, Segev et al. [13] developed 0-D models of PETEs with lumped parameters, where they only considered radiative recombination of carriers and reported a theoretical conversion efficiency of 70.4% when combining with a secondary thermal cycle. Xiao et al. [14] also established a 0-D model to assess the working performance of a PETE-Carnot system, where they reported a solar-to-electricity efficiency of 54.32% at 500 kW/m^2 incident solar flux. In these models, carrier transport was neglected and losses caused by electron recombination on the surface and the bulk were not fully considered. Varpula et al. [15] developed a 1-D model of the PETE converter to investigate its performance with Si, GaAs, and InP as the cathode, and concluded that GaAs and InP performed higher efficiencies (20–25%) than Si (10–15%). Wang et al. [16] further established a diffusion-emission model for the PETE converter with $Al_xGa_{1-x}As$/GaAs as the cathode to analyze the effects of Al element and layer thickness. Feng et al. [17] also developed a theoretical model for the $Al_xGa_{1-x}As$/GaAs cathode with an exponential-doping GaAs and a graded Al composition, where they found the conversion efficiency could be greatly improved by built-in electric fields. Liu et al. [18] proposed a GaAs nanowire cathode with an exponential doping and graded Al composition for the PETE converter, where the optimum wire length of 300–340 nm was derived based on a theoretical model. Elahi et al. [19] developed an energy balance model of PETE converters, and reported a solar-electricity efficiency of 18% for 100 × solar irradiations.

With electrons emitting through the vacuum gap, a space-charge region will form in the interelectrode gap due to the electron accumulation, which resists electron transportation and weakens output current density of the PETE converter. To take into consideration the space-charge effect, the Langmuir space-charge theory is usually adopted. Su et al. [20] analyzed the space-charge effect on current-voltage characteristics of the PETE converter and explored the effects of cathode bandgap, electron affinity, temperature, and electrode spacing on the conversion efficiency. However, the influence of the evanescent wave radiation was not considered in their work. Wang et al. [21] developed a theoretical model with the consideration of the space-charge effect and the near-field radiation between two electrodes, and managed to obtain the maximum efficiency by optimizing the operating voltage and the interelectrode gap. Datas et al. [5,22] proposed a theoretical model for the analysis of a thermionic-enhanced near-field thermophotovoltaics (nTiPV device), where they adopted the Langmuir theory to describe the space-charge region in vacuum gaps. Only a few models

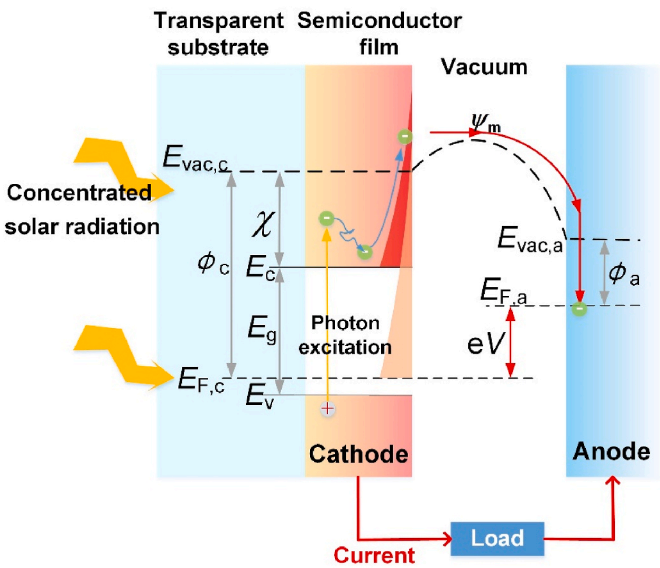

Fig. 1. Schematic of the PETE, where $E_{vac,c}$ and $E_{vac,a}$ refer to the vacuum energy levels of the cathode and the anode, respectively. $E_{F,c}$ and $E_{F,a}$ refer to the Fermi levels of the cathode and the anode, respectively. ϕ_c and ϕ_a refer to the work functions of the cathode and the anode, respectively.

comprehensively considered solar-photon absorption, electron generation and diffusion along the cathode, as well as space-charge and near-field photon tunneling effects between electrodes. In addition, using ideal cycles as tandem thermal cycle cannot reliably reflect the characteristics of the system.

To fully consider the coupling effects of electron generation and diffusion in semiconductor, the carrier recombination losses and the space-charge effect, photo-thermo-electric coupling models of the PETE converter are developed in this work. Steady-state continuity equations of both electrons and holes in the semiconductor cathode are adopted, where carrier diffusion and loss mechanisms owing to surface and bulk recombination are included. The space-charge and near-field radiation effects are also embedded. Effects of key parameters on the performance of PETE converter are analyzed in detail, and a hybrid model combining a 1-D transient Stirling cycle is further explored.

2. Mathematical model

2.1. Evaluation of the PETE converter

For the single thermionic emission of a semiconductor cathode without illumination, the emitted electron density can be calculated by Eq. (1).

$$N_{TE} = \frac{A_c T_c^2}{e} \exp\left(-\frac{\Delta E_c}{kT_c}\right) \tag{1}$$

here $A_c = 4\pi e m_n^* k^2/h^3$ is the Richardson's constant of the cathode, T_c is the cathode temperature, $e = 1.6 \times {}^{-19}$ C is the electron charge, $k = 1.38 \times 10^{-23}$ J/K is the Boltzmann's constant. $h = 6.626 \times 10^{-34}$ J·s is the Planck constant, and m_n^* is the effective mass of electrons in the conduction-band. ΔE_c is the motive barrier of the cathode that can be further expressed by Eq. (2).

$$\Delta E_c = \begin{cases} \phi_c & \text{for} \quad eV \le \phi_c - \phi_a \\ \phi_a + eV & \text{for} \quad eV > \phi_c - \phi_a \end{cases} \tag{2}$$

here V, ϕ_c and ϕ_a are the output voltage, cathode work function and anode work function, respectively.

Compared with the single thermionic emission, the PETE converter shows a significant advantage due to the combination of photonic and thermal processes, where the emitted electron density under illumination and high temperature can be calculated by Eq. (3) [11].

$$N_c = \frac{n}{n_{eq}} \cdot \frac{A_c T_c^2}{e} \exp\left(-\frac{\Delta E_c}{kT_c}\right) \tag{3}$$

here n is the conduction-band electron concentration on the emission surface under illumination, and n_{eq} is the equilibrium conduction-band electron concentration.

Similar with the single thermionic emission by the cathode, reverse electron density emitted by the anode can be calculated by Eq. (4).

$$N_a = \frac{A_a T_a^2}{e} \exp\left(-\frac{\Delta E_a}{kT_a}\right) \tag{4}$$

here $A_a = 120$ A/(cm^2·K^2) is the Richardson constant of the anode, and ΔE_a the motive barrier of the anode.

$$\Delta E_a = \begin{cases} \phi_c - eV & \text{for} \ eV \le \phi_c - \phi_a \\ \phi_a & \text{for} \ eV > \phi_c - \phi_a \end{cases} \tag{5}$$

When the space-charge effect in the interelectrode gap is neglected, the net emission current density (J) of the PETE can be expressed by Eq. (6).

$$J = e(N_c - N_a) \tag{6}$$

The output power density of the PETE converter can be calculated by Eq. (7).

$$P_{PETE} = [J(V - JSR_{lead})]_{max} \tag{7}$$

here R_{lead} is the lead resistance.

As the space-charge regime limits electron movements and deteriorates the conversion efficiency, the space-charge effect is evaluated in this work by using the Langmuir theory (Fig. S1, Eqs. (S1) – (S17)) and assuming a 1-D collisionless electron flow. In this way, the calculation of current density can be modified as shown in Eq. (8) [21].

$$J = A_c T_c^2 \frac{n}{n_{eq}} \exp\left(-\frac{\psi_m}{kT_c}\right) - A_a T_a^2 \exp\left(-\frac{\psi_m - eV}{kT_a}\right) \tag{8}$$

here ψ_m is the maximum electron motive in the interelectrode gap when taking the cathode Fermi level as the zero reference point. On the right side of Eq. (8), the first term refers to the current density from cathode to anode (J_c) and the second term refers to the current density from anode to cathode (J_a). The corresponding emitted electron densities can be calculated by $N_c = J_c/e$ and $N_a = J_a/e$. n/n_{eq} is called photon enhancement factor that can be used as a quantitative performance metric of photon enhancement [12]. A desirable photon enhancement mode performs $n/n_{eq} > 1$. Otherwise, the converter exhibits pure thermionic mode, even seems destroy thermionic current when $n/n_{eq} < 1$.

According to the first law of thermodynamics, the cathode temperature is determined by the energy balance equation of the cathode as shown in Eq. (9).

$$Q_{sun} - Q_{rad,C\_amb} - Q_{rad,C\_A} - Q_{rad,recom} - Q_{electron} - Q_{lead} - Q_{penetrate} = 0 \tag{9}$$

here $Q_{rad,\,C\_amb}$ is the radiative heat loss from the cathode to the ambient that can be calculated by the Stefan-Boltzmann law. $Q_{electron}$ is the energy transferred by thermionic electrons that can be further expressed by Eq. (10).

$$Q_{electron} = N_c(\psi_m + 2kT_c) - N_a(\psi_m + 2kT_a) \tag{10}$$

Q_{rad,C_A} is the near-field (or far-field) radiative heat loss between the two electrodes, which is contributed by both the propagating-wave and the evanescent-wave photons (near-field photon tunneling). The evanescent-wave photons tunnel via micro/nanoscale vacuum and leads to significant heat transfer [23]. The detailed calculation of is described in Eqs. (S18) – (S31). Incident energy obtained by the cathode of sunlight is calculated in terms of AM1.5 direct + circumsolar spectrum as expressed in Eq. (11).

$$Q_{\text{sun}} = C\int_0^{\infty} \Omega(\lambda)d\lambda \tag{11}$$

here $\Omega(\lambda)$ represents the solar photon energy flux density per wave length of AM1.5 direct + circumsolar spectrum, and C is the concentration ratio. $Q_{\text{penetrate}}$ is the solar energy penetrating through the cathode. $Q_{\text{rad, recom}}$ is the radiative energy of emitted blackbody photons above the bandgap, which can be estimated by Eq. (12) at the non-equilibrium condition [11].

$$\begin{aligned} Q_{\text{rad,recom}} &= \left[e^{\left(E_{\text{F,n}}-E_{\text{F,p}}\right)/kT_{\text{c}}} - 1\right]\frac{2\pi}{h^3c^2}\int_{E_g}^{\infty}\frac{(hv)^3}{\exp\left(\dfrac{hv}{kT_{\text{c}}}\right)-1}d(hv) \\ &= \left(\frac{np}{n_{\text{eq}}p_{\text{eq}}}-1\right)\frac{2\pi}{h^3c^2}\int_{E_g}^{\infty}\frac{(hv)^3}{\exp\left(\dfrac{hv}{kT_{\text{c}}}\right)-1}d(hv) \end{aligned} \tag{12}$$

here h is the Planck's constant and c is the speed of light. Q_{lead} is the heat loss in the lead that can be calculated by the Wiedemann-Franz law and Joule's law as shown in Eq. (13) [3,5].

$$Q_{\text{lead}} = \frac{L}{2SR_{\text{lead}}}\left(T_{\text{c}}^2 - T_{\text{a}}^2\right) - \frac{1}{2}SR_{\text{lead}}J^2 \tag{13}$$

The waste energy from the anode Q_{anode} is evaluated base on the thermal balance principle as shown in Eq. (14).

$$Q_{\text{anode}} = Q_{\text{rad,C\_A}} + Q_{\text{electron}} + \frac{1}{2}Q_{\text{rad,recom}} + Q_{\text{lead}} + Q_{\text{penetrate}} - P_{\text{PETE}} - Q_{\text{rad,A\_amb}} \tag{14}$$

here we assume that the probability of photons emitted from both sides of the cathode due to electron radiative recombination is equal, that is, half of $Q_{\text{rad, recom}}$ is considered to be absorbed by the anode. $Q_{\text{rad, A\_amb}}$ is the radiative heat loss from the anode to the ambient.

Therefore, power conversion efficiency (PCE, marked as η_{PETE}) of the PETE converter can be calculated by Eq. (15).

$$\eta_{\text{PETE}} = \frac{P_{\text{PETE}}}{Q_{\text{sun}}} \tag{15}$$

The power conversion efficiency of the hybrid system (tandem with the Stirling cycle) can be further calculated by Eq. (16).

$$\eta = \frac{P_{\text{PETE}} + P_{\text{SE}}/S}{Q_{\text{sun}}} \tag{16}$$

here P_{SE}/S is the output power of the Stirling engine per unit area of the PETE converter, which is called as the output power density of Stirling engine. P_{SE} is the output power of the Stirling engine, and S denotes the working area of the PETE converter to match the working condition of a Stirling engine as shown in Eq. (17).

$$S = \frac{Q_{\text{SE}}}{Q_{\text{a,net}}\eta_{\text{anode-SE}}} \tag{17}$$

here Q_{SE} is the required heating power of the Stirling engine, and $\eta_{\text{anode-SE}}$ is the utilization efficiency of the PETE waste heat by considering the heat transfer loss. A well-developed Stirling engine model [24,25] is adopted as a sub-model to analyze the Stirling cycle in the combined power generation system. Related information can be found in Eqs. (S31) - (S40).

2.2. Modeling of the semiconductor cathode

Distribution of carrier concentration is the key basis for the performance evaluation of PETE converter. In this work, a 1-D model is developed to study the photo-thermo-electric characteristics of the semiconductor cathode. The generation, the diffusion, the emission and the loss mechanisms of non-equilibrium carriers are considered. Both conduction-band electrons and valence-band holes are taken into consideration, and carrier distributions can be obtained by solving 1-D transport equations of the semiconductor cathode as shown in Eq. (18) and Eq. (19).

$$-D_n\frac{d^2\Delta n}{dx^2} = G - R \tag{18}$$

$$-D_p\frac{d^2\Delta p}{dx^2} = G - R \tag{19}$$

here $\Delta n = n - n_{\text{eq}}$ and $\Delta p = p - p_{\text{eq}}$ are the non-equilibrium electron concentration of conduction-band and the hole concentration of valence-band, respectively. Accordingly, n_{eq} and p_{eq} are equilibrium concentrations of the electron and the hole, and D_{n} (D_{p}) denotes electron (hole) diffusion coefficient. According to Einstein's relationship, $D_n = kT\mu_n/e$ and $D_p = kT\mu_p/e$.

A super-bandgap photon can excite the valence-band electrons to the conduction-band. The photon excitation rate of the conduction-band electrons per unit volume can be expressed by the rate of photon absorption with energy greater than the bandgap as shown in Eq. (20).

$$G(x) = C\int_0^{\lambda_0}\frac{\Omega(\lambda)}{hc/\lambda}\cdot\alpha(\lambda)\cdot e^{-\alpha(\lambda)x}d\lambda \tag{20}$$

here x is a 1-D coordinate with the light-incident surface as the origin, $\Omega(\lambda)$ represents the solar photon energy flux density per wave length of AM1.5 direct + circumsolar spectrum, and $\alpha(\lambda)$ refers to the absorption coefficient for photons with wavelength λ. The boundary conditions of the transport equations are set as given in Eqs. (21) – (24).

$$-D_n\frac{d\Delta n}{dx}\bigg|_{x=0} = -S_{n,0}\Delta n(0) \tag{21}$$

$$-D_n\frac{d\Delta n}{dx}\bigg|_{x=t} = S_{n,t}\Delta n(t) + N_{\text{c}} - N_{\text{a}} \tag{22}$$

$$-D_p\frac{d\Delta p}{dx}\bigg|_{x=0} = -S_{p,0}\Delta p(0) \tag{23}$$

$$-D_p\frac{d\Delta p}{dx}\bigg|_{x=t} = S_{p,t}\Delta p(t) \tag{24}$$

here $S_{n,0}$ and $S_{n,t}$ are the surface recombination rates on the photon incident surface and the electron emission surface, and t is the film thickness. It should be noted that reversal electrons absorbed on the cathode surface contributes to the cathode conduction-band concentration, which is already considered in Eq. (22).

There is also recombination in the bulk of cathode while generating electrons. Radiative, Shockley-Read-Hall (SRH) and Auger recombination types are taken into consideration, as expressed in Eq. (25).

$$R = R_{\text{rad}} + R_{\text{Auger}} + R_{\text{SRH}} \tag{25}$$

For an equilibrium semiconductor, the radiative recombination rate can be determined by the rate of photon emitted per unit area as shown in Eq. (26) [11].

$$R_0 = \frac{2\pi}{h^3c^2}\int_{E_g}^{\infty}\frac{(hv)^2}{\exp\left(\frac{hv}{kT_{\text{c}}}\right)-1}d(hv) \tag{26}$$

The photon emission rate can be exponentially enhanced for non-equilibrium conditions according to Boltzmann statistics as shown in Eq. (27).

$$R_0^{'} = \left(\frac{np}{n_{eq} p_{eq}} - 1 \right) R_0 \quad (27)$$

Therefore, radiative recombination rate per unit volume can be calculated by Eq. (28).

$$R_{rad} = \left(\frac{np}{n_{eq} p_{eq}} - 1 \right) \frac{R_0}{t} \quad (28)$$

In a p-type semiconductor, the Auger recombination rate can be calculated by Eq. (29) [11,26].

$$R_{Aug} = C_n \left(n^2 p - n_{eq}^2 p_{eq} \right) + C_p \left(np^2 - n_{eq} p_{eq}^2 \right) \quad (29)$$

Finally, the SRH recombination rate can be obtained by Eq. (30) [26].

$$R_{SRH} = \frac{np - n_{eq} p_{eq}}{\tau_{SRH,n} \left(p + n_{eq} \right) + \tau_{SRH,p} \left(n + p_{eq} \right)} \quad (30)$$

here $\tau_{SRH,n}$ and $\tau_{SRH,p}$ are the SRH lifetimes for electrons and holes, respectively.

Equilibrium electron concentration in conduction-band n_{eq} and equilibrium hole concentration in valence-band p_{eq} are also required in the model. For p-type semiconductors, the Fermi level can be obtained according to the charge neutrality criterion, expressed by Eq. (31) [11].

$$N_C \exp\left(- \frac{E_g - E_F}{kT_c} \right) + N_A \frac{1}{1 + 4 \exp\left(\frac{E_A - E_F}{kT_c} \right)} = N_V \exp\left(- \frac{E_F}{kT_c} \right) \quad (31)$$

here N_C and N_V are the effective density of states in the conduction band and valence band, respectively. N_A and E_A are impurity acceptor concentration and impurity energy level, respectively. The energy level here takes the valence band maximum as the zero reference. N_C and N_V can be calculated by Eqs. (32) and (33), respectively.

$$N_C = 2 \left(\frac{2\pi m_n^* k T_c}{h^2} \right)^{\frac{3}{2}} \quad (32)$$

$$N_V = 2 \left(\frac{2\pi m_p^* k T_c}{h^2} \right)^{\frac{3}{2}} \quad (33)$$

here m_n^* and m_p^* are the effective mass of electrons at the conduction band minimum and the effective mass of holes at valence band maximum, respectively. The equilibrium electron concentration in conduction band and the equilibrium hole concentration in valence band can be obtained by Eqs. (34) and (35), respectively.

$$n_{eq} = N_C \exp\left(- \frac{E_C - E_F}{kT_c} \right) \quad (34)$$

$$p_{eq} = N_V \exp\left(\frac{E_F - E_V}{kT_c} \right) \quad (35)$$

If the electron affinity χ of the cathode is given, the work function can be calculated by Eq. (36).

$$\phi_c = E_g + \chi - E_F \quad (36)$$

Main properties of the GaAs cathode for the model development are listed in Table 1.

Table 1
Main properties of GaAs cathode used in the simulation.

Parameter	Value or model
Bandgap, E_g	[a] [27]
Spectral photon absorption coefficient, α	[a] [15,27]
Electron and hole mobilities, μ_e and μ_h	[a] [28]
Doping density, N_A	1×10^{19} cm^{-3}
Impurity energy level, E_A	0.02 eV [12]
Effective mass of electrons at conduction band minimum, m_n^*	0.067 m_e [10,26]
Effective mass of holes at valence band maximum, m_p^*	0.47 m_e [26]
Electron Auger recombination coefficient, C_n	1.6×10^{-29} cm^6/s [15]
Hole Auger recombination coefficient, C_p	4.6×10^{-31} cm^6/s [15]
Electron and hole SRH lifetime, $\tau_{SRH,n}$ and $\tau_{SRH,p}$	both 1×10^{-6} s [29]
Carrier surface recombination rate on light incident surface, $S_{n,0}$ and $S_{p,0}$	both 100 cm/s [12,30]
Carrier surface recombination rate on emitting surface, $S_{n,t}$ and $S_{p,t}$	both 0 cm/s [12,26]
Dielectric function	[a] [31]

[a] Data or model acquired from the cited references.

3. Results and discussion

3.1. Effects of solar concentration and cathode properties

Solar concentration and cathode parameters (e.g., electron affinity, bandgap, work function, thickness and recombination rate) are crucial to working temperature and emitted electrons of PETE converters. Solar concentration ratio refers to the concentration multiple of solar radiation. In this section, detailed studies are conducted to investigate their effects and the main parameters are listed in Table 2. Fig. 2(a) and (b) shows the saturation current density and the photon enhancement factor n/n_{eq} of the PETE converter as a function of solar concentration ratio. For convenience, $J_{TE} = e \times N_{TE}$ is recorded as the thermionic current density and J_{PETE} as the total current density of the PETE converter. $J_{PE} = J_{PETE}$ - J_{TE} is called the photo-enhanced current density. It shows that J_{PETE} monotonically increases from 0.11 to 17.88 A/cm^2 with the increase of solar concentration ratio from 50 to 500. Meanwhile, the cathode temperature increases from 997 to 1337 K with a gradually decreasing growth rate, as shown in Fig. 2(c) blue line, and the work function correspondingly varies from 1.89 to 1.62 eV. Fig. 2(a) demonstrates that J_{TE} increases exponentially with a gradually increased proportion of J_{PETE}. However, the photon enhancement factor n/n_{eq} gradually decreases from 46 to 1.5. The PETE converter performs from photon-enhanced mode towards pure thermionic mode. The proportion of J_{PE} drops to <0.5 after 300 suns, and only 0.33 at 500 suns.

For comparison, Fig. 2(b) shows results without considering the Auger recombination, where J_{PETE} increases from 0.18 to 18.39 A/cm^2 with the increase of solar concentration ratio from 50 to 500. The contribution of J_{PE} still accounts for 0.72 at 500 suns and the corresponding photon enhancement factor is 3.62. This advanced performance is contributed by two aspects. On the one hand, the pure thermionic current is relatively low when without considering the Auger recombination, owing to the low temperature and the high work function of the cathode, as shown in Fig. 2(c). On the other hand, the conduction-band electrons are accompanied by recombinations in the process of diffusing to the emitting surface. Only electrons that reach the emitting surface before recombination have a chance to be emitted. The conduction-band electron concentration on the emitting surface is higher when without considering the Auger recombination, thus leading to a more significant photon enhancement effect (i.e. larger n/n_{eq}).

Fig. 2(d) illustrates that both the power conversion efficiency PCE

Table 2
Main parameters used in the simulation.

Parameter	Value
Solar concentration, C	50–500
Cathode material	GaAs
Cathode thickness, t	0.1–100 μm
Electron affinity, χ	0.2–1.6 eV
Anode work function, ϕ_a	0.9 eV
Anode temperature, T_a	500 K
Interelectrode spacing, d	1 μm

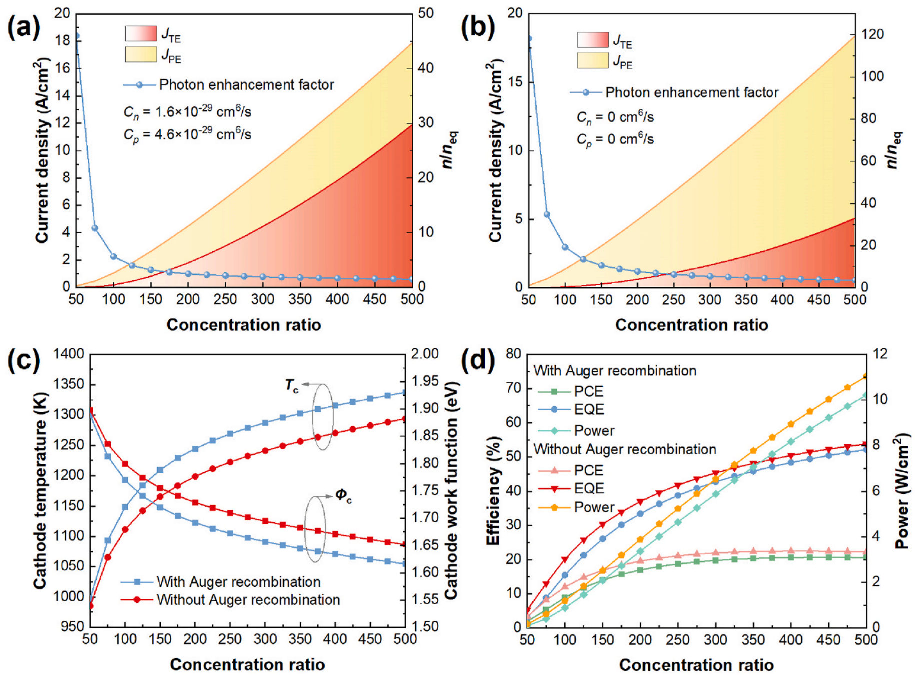

Fig. 2. Performance metric variations as a function of solar concentration ratio. The current density and photon enhancement factor of the PETE converter **(a)** with and **(b)** without considering the Auger recombination, respectively. **(c)** The cathode temperature and the cathode work function. **(d)** The power conversion efficiency PCE and the external photon efficiency EQE of the PETE converter as a function of solar concentration, where the EQE here refers to the ratio of effective emitted electrons to the incident photons. For each case, the operating voltage is optimized for the maximum power output point (MPP). In the case of panel (a), the Auger recombination coefficients for electrons and holes are 1.6×10^{-29} cm^6/s and 4.6×10^{-29} cm^6/s, respectively. In the case of panel (b), the Auger recombination coefficient for electrons and holes are both 0.

and the external photon efficiency EQE of the PETE converter can be improved if Auger recombination is eliminated. The corresponding PCE and EQE obtain 22.24% and 53.83%, respectively, at the solar concentration of 500. This quantitatively shows the Auger recombination has an important influence on the performance of PETE converter.

Band gap and electron affinity affect the work function and the performance of PETE converters together, as shown in Eq. (36). The former is the barrier that needs to be overcome to excite the valence band electrons to the conduction band. The latter is the barrier that needs to be overcome to emit conduction-band electrons from cathode surface. To study single effect of the band gap, the cathode work function is stabilized at 1.8 eV in Fig. 3 by adjusting the electron affinity. The conversion efficiencies first increases and then decreases with the increase of the band gap, obtaining maximum values > 20%. The optimum band gap changes from 1.5 to 1.35 eV when solar concentration ratio varies from 100 to 500.

The trends of the conversion efficiency with the band gap can be explained as follows. As the band gap increases, the photon enhancement factor increases significantly (Fig. 3(b)), leading to an increased current and thus conversion efficiency. The increased current causes an

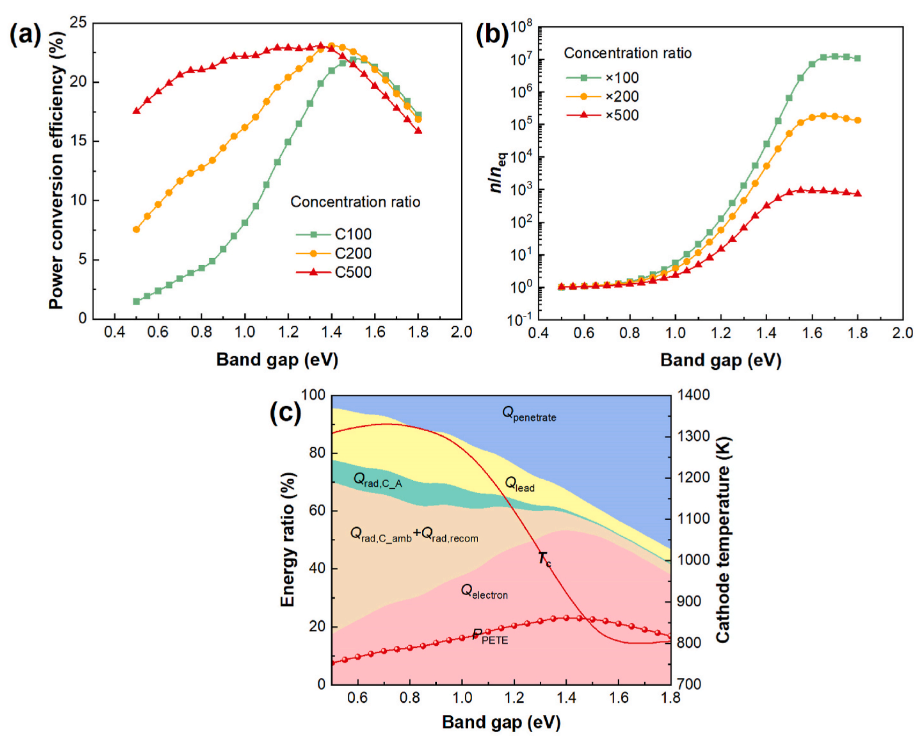

Fig. 3. **(a)** The conversion efficiency and **(b)** the photon enhancement factor change as a function of the band gap for different solar concentration ratios.

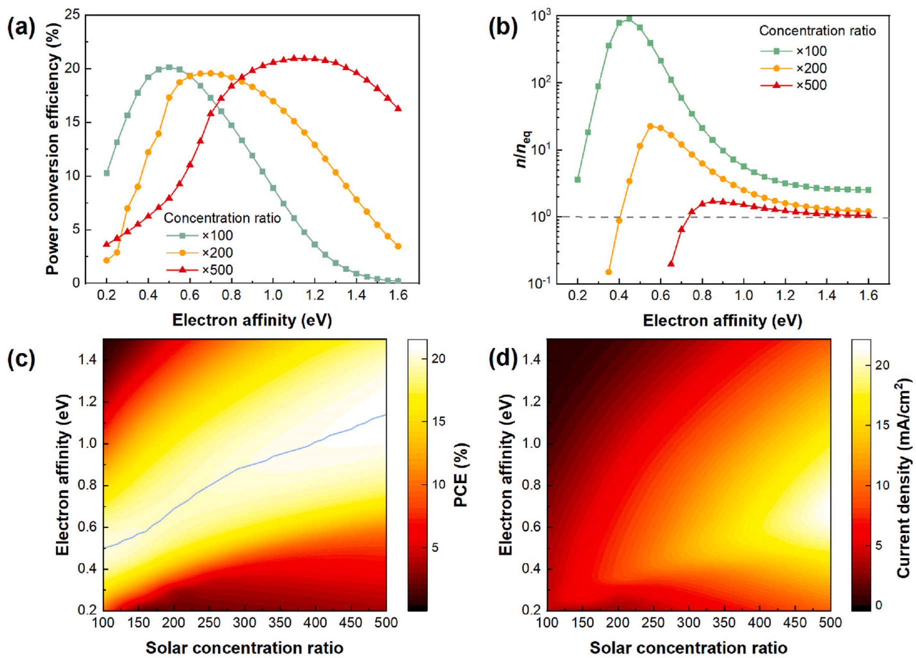

Fig. 4. Performance metric variations with the electron affinity and solar concentration ratio. **(a)** The conversion efficiency and **(b)** the photon enhancement factor change as a function of the electron affinity. **(c)** The conversion efficiency and **(d)** the current density change as a function of the electron affinity and solar concentration ratio. The blue line plots the optimal thickness as a function of solar concentration ratio. (For interpretation of the references to colour in this figure legend, the reader is referred to the Web version of this article.)

increased thermionic heat flow $Q_{electron}$ (Fig. 3(c)). In addition, it should be noted that photon absorption coefficient is closely related to the band gap in the model [15,27]. As a result, the cathode absorbed solar photons reduced sharply as the band gap increases. Therefore, the cathode temperature decreases dramatically, so as the intrinsic thermionic current. The increase of photon enhancement plays a leading role for band gap lower than the optimum value and the conversion efficiency increases with the band gap. The decrease of intrinsic thermionic current makes a more impact when the band gap continues to increase, which explains the decrease process of the conversion efficiency. Results show that the optimal band gap under different solar concentration ratios is around 1.4 eV. Fig. S1 gives the performance metric variations as a function of solar concentration ratio for the band gap of 1.4 eV.

Electron affinity can be engineered by surface adsorption of alkali metal atoms (e.g., Cs, Ba) and Cs/O activation [11,32]. Fig. 4 illustrates that the conversion efficiency increases first and then decreases with the appearance of an optimum electron affinity. The maximum conversion efficiency is ~20% for all solar concentration ratios and the optimal electron affinity increases from 0.5 to 1.14 eV as solar concentration ratio varies from 100 to 500. The photon enhancement factor also experiences an increase-decrease process. Fig. 4(d) shows that the electron affinity for maximum current density is much lower than the optimum electron affinity. The output voltage is also affected by the electron affinity and a trade-off between current and voltage can be adjusted by choosing the optimum electron affinity. Fig. S2 gives trends of the power density, the voltage, the cathode temperature, and the photon enhancement factor with the electron density and solar concentration ratio.

Thickness is another key parameter of the cathode. Fig. 5(a) shows the conversion efficiency and the photon enhancement factor variation as a function of cathode thickness for the solar concentration of 100, 200, and 500, respectively. It can be seen that the conversion efficiency increases first and then decreases slowly with the appearance of an optimum cathode thickness. The photon enhancement factor shows a sharply downward trend with the cathode thickness. Fig. 5(b) shows variations of each energy density and the cathode temperature with the cathode thickness for the solar concentration ratio of 200. The penetrating solar energy $Q_{penetrate}$ decreases quickly as the cathode thickness increases from 0.1 to 1 μm, whereas $Q_{penetrate}$ keeps nearly unchanged as the cathode thickness continues to increase. The $Q_{electron}$ occupies the largest proportion, part of which is converted to the output power P_{PETE}. The rest heat of $Q_{electron}$ is transferred to the anode as the waste heat. $Q_{electron}$ increases first and then steady near unchanged with increasing of the cathode thickness. Terms of Q_{lead}, Q_{rad,C_A} and $Q_{rad,\ C\_amb} + Q_{rad,\ recom}$ shows a similar trend to that of $Q_{electron}$. Non-radiative recombinations of photon-excited electrons during diffusion towards the emitting surface increases with increasing the cathode thickness. The cathode temperature increases due to the increase of both absorbed solar energy and non-radiative recombination thermalization.

The performance of the PETE converter is limited by a trade-off between solar energy absorption and photon enhancement, which can be regulated by changing the cathode thickness. Increasing the thickness of the cathode can enhance the utilization of photons, but it also increases the loss during the electron diffusion process. Therefore, it is necessary to optimize the thickness for specific cathode properties by considering the photon absorption coefficient, the bulk diffusion coefficient, the electron mobility, and the electron recombination rate. Fig. 5(c) demonstrates the optimal thickness increases from 0.78 to 1.52 μm as solar concentration ratio increases from 50 to 500, and a desirable thickness range of 0.5–1.5 μm is recommended. Fig. 5(d) indicates the device operates in high photon-enhanced mode for the recommended thickness range. Trends of the power density, the voltage, the cathode temperature, and the photon enhancement factor with the cathode thickness and the solar concentration ratio are shown in Fig. S3.

3.2. *Interelectrode spacing and space-charge effect*

The space-charge effect restricts number of the effective electrons reaching the anode surface, which can be adjusted by interelectrode spacing and output voltage. In this section, detailed studies are

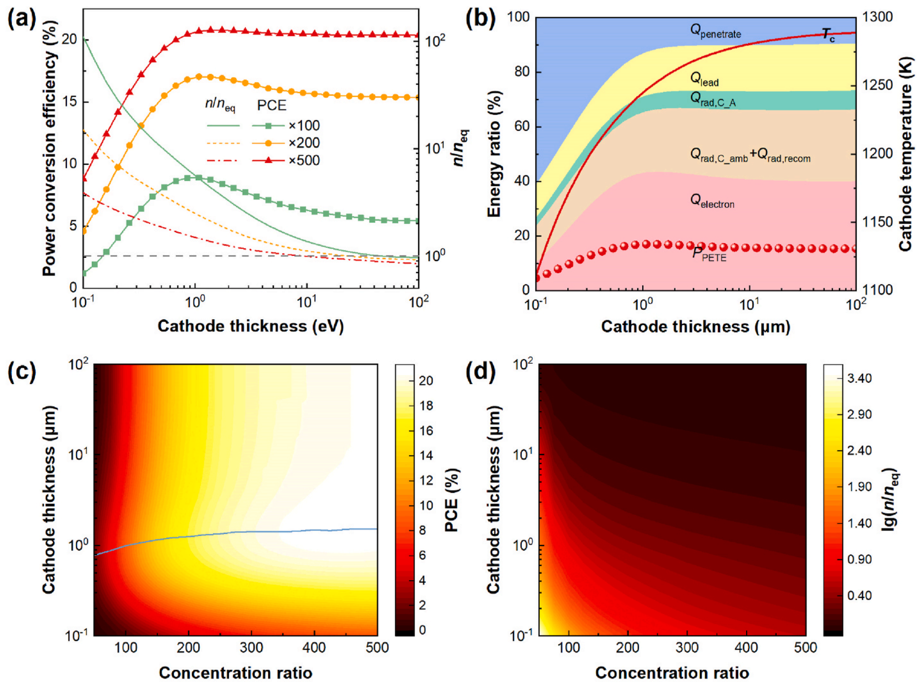

Fig. 5. Performance metric variations with the cathode thickness and the solar concentration ratio. **(a)** The conversion efficiency and the photon enhancement factor change as a function of the electron affinity for different solar concentration ratios. **(b)** The energy ratio and the cathode temperature change as a function of the cathode thickness for the solar concentration of 200. **(c)** The conversion efficiency and **(d)** the photon enhancement factor changes as a function of the cathode thickness and solar concentration ratio. The blue line plots the optimal thickness as a function of solar concentration ratio. (For interpretation of the references to colour in this figure legend, the reader is referred to the Web version of this article.)

Table 3
Main parameters used in the simulation.

Parameter	Value
Solar concentration, C	500
Cathode material	GaAs
Cathode thickness, t	1 μm
Cathode electron affinity, χ	1 eV
Anode work function, ϕ_a	0.9 eV
Anode temperature, T_a	500 K
Interelectrode spacing, d	0.1–20 μm

conducted to investigate the interelectrode spacing and the output voltage of the PETE converter. Table 3 lists the main parameters used in the simulation. As shown in Fig. 6(a), the conversion efficiency first increases to a platform and then decreases with the increase of the interelectrode spacing, where it reaches the maximum values of 9.1% and 17.6% at ~1 μm for the solar concentration ration of 100 and 200, respectively. The increasing process is mainly contributed by the significant decrease of Q_{rad,C_A} with the increase of the interelectrode spacing as shown in Fig. 6(b). At a larger interelectrode spacing (>2 μm), the space-charge effect is significantly enhanced with the increase of interelectrode spacing (Fig. 7(d)), which restrains the power density and decreases the conversion efficiency. With the near-field radiation gradually transforming into the far-field radiation, the Stefan-Boltzmann law can approximately describe Q_{rad,C_A} for the interelectrode spacing >1 μm so it only depends on the temperature. For comparison, $Q_{rad,\ C\_amb}$ increases with the electrode spacing in the whole range due to the increasing cathode temperature. $Q_{penetrate}$ and Q_{lead} almost remains a constant value. Similar to the conversion efficiency, the variation trends of both $Q_{electron}$ and P_{PETE} experience an increase-platform-decrease period. A desirable interelectrode spacing range of 0.5–2 μm is recommended because all metrics shown in Fig. 6 keeps nearly unchanged and the conversion efficiency is close to the maximum value.

The effects of interelectrode spacing on the current density and the power density at different operating voltages are presented in Fig. 7. At small interelectrode spacings, three working regimes are observed, i.e., saturation regime, retarding regime, and space-charge limited regime (Fig. S4, Eqs. (S15) – (S17)). While the theoretical saturation voltage is < 0 and saturation regime is missing at large interelectrode spacings (10 μm).

To overcome the energy barrier caused by the space-charge effect, a bias voltage can be applied to change the operating voltage and regulate the current density. Fig. 7(c) shows the trends of energy flows and the

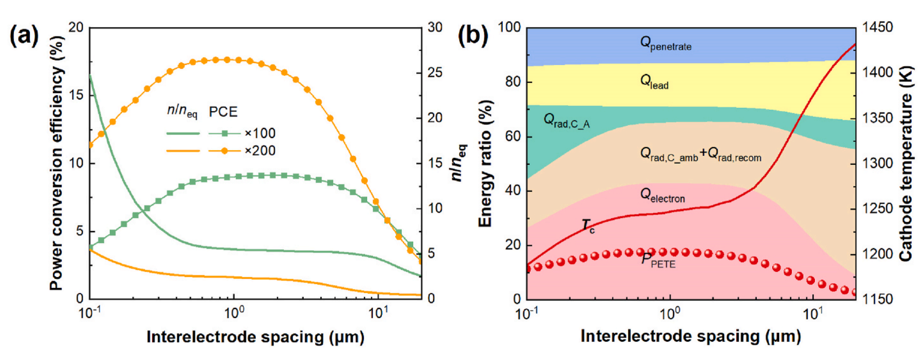

Fig. 6. Performance metric variations with the interelectrode spacing. **(a)** The conversion efficiency and the photon enhancement factor change as a function of the interelectrode spacing for different solar concentration ratios. **(b)** The energy ratio and the cathode temperature change as a function of the interelectrode spacing for the solar concentration of 200.

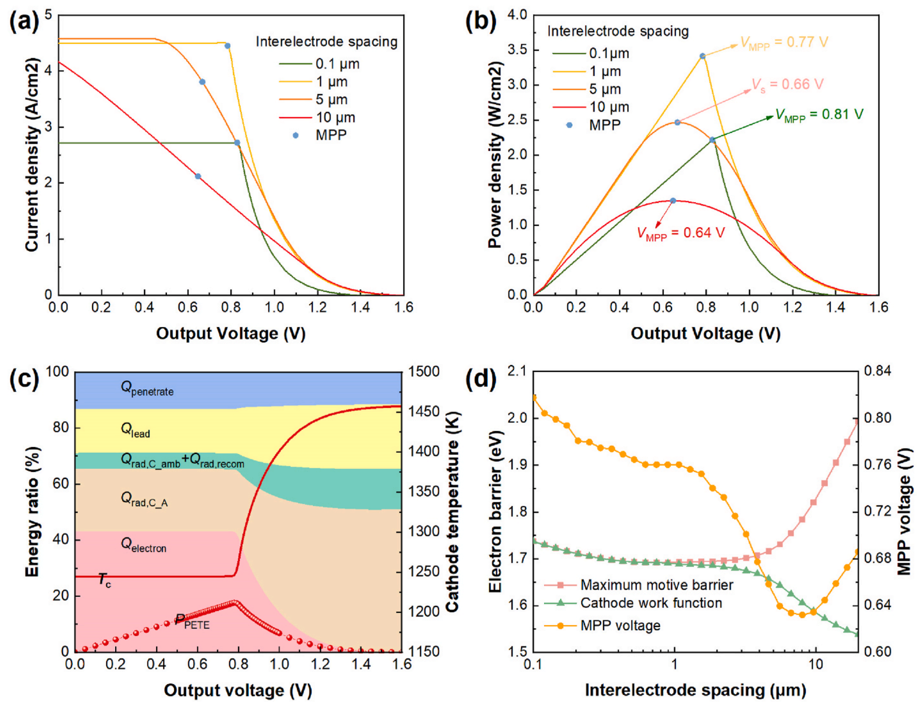

Fig. 7. Performance metric variations with the output voltage and the interelectrode spacing. **(a)** *J-V* and **(b)** *P–V* diagrams for the interelectrode spacing of 0.1, 1, 5, and 10 μm. **(c)** The energy ratio and the cathode temperature change as a function of the output voltage for the interelectrode spacing of 1 μm. **(d)** The maximum motive barrier, the cathode work function and the MPP voltage as a function of the interelectrode spacing. The solar concentration ratio in this case is 200.

cathode temperature with the output voltage for the interelectrode spacing of 1 μm and the solar concentration ration of 200. In this case, the MPP voltage V_{MPP} is close to the saturation voltage V_s. For $V < V_{MPP}$, all terms of heat flow and the cathode temperature keep unchanged, while the output power density increases dramatically. For $V > V_{MPP}$, the current density is dramatically lowered with the voltage increasing, so as the heat flow $Q_{electron}$, caused by the increase of the maximum electron barrier between the electrodes. Q_{rad,C_A}, $Q_{rad,\ C\_amb}$, $Q_{rad,\ recom}$, and Q_{lead} are raised for the increasing cathode temperature. The operating voltage is optimized for a PETE converter to obtain the maximum efficiency (output power) as shown in Fig. 7(d). With the increase of the interelectrode spacing, V_{MPP} decreases from 0.82 eV at 100 nm to 0.63 V at 8 μm, and then increases to 0.69 V at 20 μm. It is also observed that V_{MPP} keeps at the space-charge limited regime ($>V_s$) for the interelectrode spacing range >1 μm.

Rahman et al. [33] used similar space-charge and near-field radiation model to study working characteristics of a thermionic converter. However, they further considered imperfect electron absorption by the collector, which, as they reported, will decreases the maximum conversion efficiency and optimum interelectrode spacing. It should be noted that electron tunneling current and image charge perturbation were not considered in the present work, which may cause additional errors when the interelectrode spacing is reduced to nanoscale. Jensen et al. [19,34] took these factors into consideration when researching a submicrometer-gap thermionic converter and the corresponding method can be applied to improve the present model.

3.3. Hybrid PETE-stirling cycle system

To recover the waste heat of PETE converters, a hybrid system combining the Stirling cycle is constructed and numerically analyzed, as shown in Fig. 8(a). GPU-3 built by General Motors Research Laboratories is used, of which the main working parameters are listed in Table 4 [35]. As shown in Fig. 8(b) and (c), the power density of the Stirling engine is raised from 30.91 to 90.09 kW/m^2, while for the PETE it drops from 102.13 to 41.18 kW/m^2 with the increase of anode temperature from 500 to 900 K, under the solar concentration ratio of 500. The highest system power density (162.65 kW/m^2) is obtained at 660 K anode temperature with 32.77% conversion efficiency, where the power density contributed by the PETE and the Stirling engine are 96.1 kW/m^2 and 66.55 kW/m^2, respectively. It is also observed that the power ratio decreases from 3.3 to 0.43, indicating the increase of the Stirling engine contribution. The decrease of PETE power density can be explained by Fig. 8(d), where J_a grows quickly and MPP output voltage reduces with the anode temperature.

Energy flows of the hybrid system at the optimal anode temperature are further presented in Fig. 9. Incident energy losses caused by the radiative recombination $Q_{rad,\ recom}$ and the thermal radiation to the ambient $Q_{rad,\ C\_amb}$ are 1.91%, and 11.31%, respectively. 65.5% of the incident energy is carried away from the cathode by thermionic electrons, i.e. $Q_{electron}$, 19.36% of the incident energy can be directly converted into the electricity P_{PETE} by the PETE converter, and the rest 46.14% is transferred to the anode in the form of thermalization. Another portion of the incident energy is transferred to the anode through the cathode penetrating solar photon (12.43%), the near-field radiation Q_{rad,C_A} (3.63%) and the lead loss (4.90%). As a result, the rest 67.42% of incident energy can utilized in the form of heat by the Stirling engines. In this way, the GPU-3 engines can further output 13.41% more electricity and the system can yield a total output power of 162.65 kW/m^2 with a conversion efficiency of 32.77%.

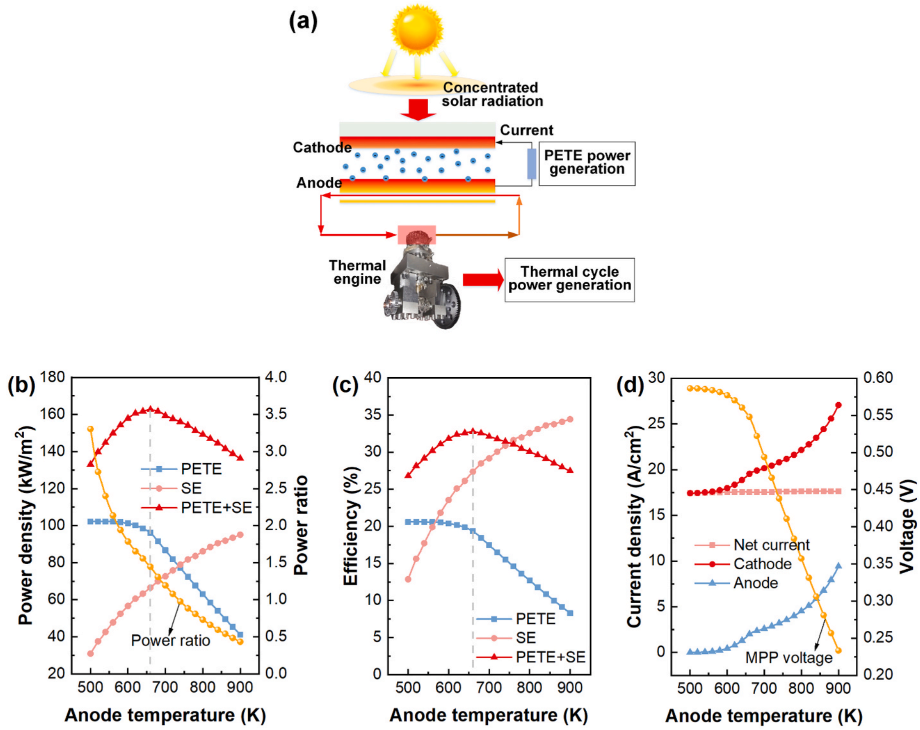

Fig. 8. **(a)** Schematic of a PETE-Stirling system. **(b)** Power densities, **(c)** conversion efficiencies, and **(d)** current densities of the PETE-Stirling system as a function of the anode temperature. The power ratio is defined as the ratio of output power density of the PETE converter to that of the Stirling engine.

Table 4
Main parameters used in the simulation.

Parameter		Value
PETE converter	Solar concentration, *C*	500
	Cathode material	GaAs
	Cathode thickness, *t*	1 μm
	Anode work function, φ_a	0.9 eV
	Anode temperature, T_a	500–900 K
	Interelectrode spacing, *d*	1 μm
Stirling engine	Type	GPU-3
	Working gas	hydrogen
	Charged pressure	2 MPa
	Rotary speed	2000 rpm
	Cooling temperature	288 K

4. Conclusions

In this work, numerical models of the PETE converter were developed with a fully consideration of the optical, the thermodynamic and the electrical aspects. Effects of key parameters on the performance of PETE converters were studied, and a hybrid PETE-Stirling system was further discussed.

We found the bandgap, the electron affinity and the cathode thickness played important roles in the performance and design of the PETE converter, where the optimal bandgap range was within 1.35–1.5 eV. The PETE conversion efficiency kept ~20% with the optimal electron affinity increases from 0.5 to 1.14 eV as solar concentration ratio varied from 100 to 500. The cathode thickness affected the performance of PETE converter by changing both solar absorption and photon enhancement. The cathode thickness should be optimized for each solar incident conditions. The interelectrode gap also significantly affected the performance of PETE converter by regulating both the space-charge effect and near-field radiation. By combining with a Stirling cycle, the hybrid system could yield a power density of 162.65 kW/m^2 with a 32.77% conversion efficiency at the 500 × AM1.5 spectrum irradiance.

The bandgap of practical materials (e.g. GaAs, InP, Si) are temperature-dependent and decrease greatly with the increase of temperature and deteriorate the performance of PETE. Thus, extensive studies are still needed to optimize the cathode material with appropriate bandgap, thickness, doping concentration, and work function. It is worth noting that GaAs tends to decomposed at high temperature. It is also of great significance to explore semiconductors suitable for PETE cathodes that work stably at high temperatures.

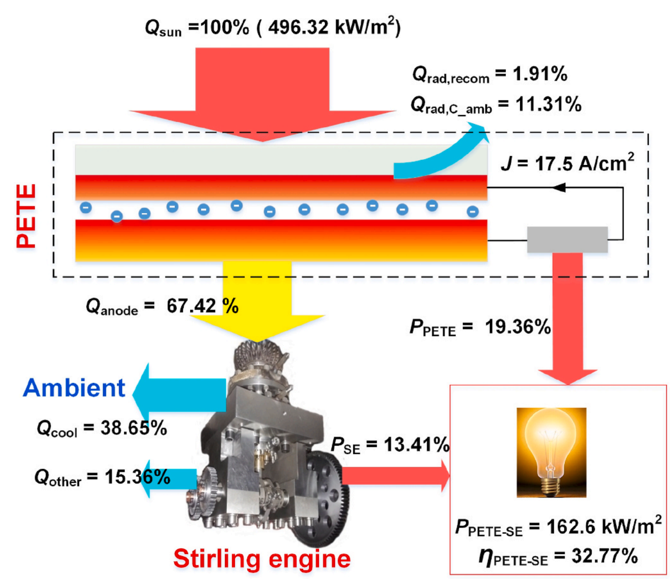

Fig. 9. Energy flow diagrams of the PETE-Stirling cycle system with CSP under the solar concentration ration of 500.

CRediT authorship contribution statement

Hao Qiu: Conceptualization, Methodology, Software, Validation, Formal analysis, Visualization, Investigation, Data curation, Writing - original draft, Writing - review & editing. **Haoran Xu:** Writing – review & editing. **Mingjiang Ni:** Supervision. **Gang Xiao:** Supervision, Project administration, Funding acquisition.

Declaration of competing interest

The authors declare the following financial interests/personal relationships which may be considered as potential competing interests: Gang Xiao reports financial support was provided by Zhejiang Provincial Natural Science Foundation. Gang Xiao reports financial support was provided by National Natural Science Foundation of China.

Data availability

The data that has been used is confidential.

Acknowledgement

The authors gratefully acknowledge the support from the Zhejiang Provincial Natural Science Foundation (NO. LR20E060001) and the Innovative Research Groups of the National Natural Science Foundation of China (NO. 51621005).

Appendix A. Supplementary data

Supplementary data to this article can be found online at https://doi.org/10.1016/j.solmat.2022.111922.

References

[1] G. Huang, K. Wang, C.N. Markides, Efficiency limits of concentrating spectral-splitting hybrid photovoltaic-thermal (PV-T) solar collectors and systems, Light Sci. Appl. 10 (2021) 28, https://doi.org/10.1038/s41377-021-00465-1.
[2] J. Fang, H. Wu, T. Liu, Z. Zheng, J. Lei, Q. Liu, H. Jin, Thermodynamic evaluation of a concentrated photochemical–photovoltaic–thermochemical (CP-PV-T) system in the full-spectrum solar energy utilization, Appl. Energy 279 (2020), 115778, https://doi.org/10.1016/j.apenergy.2020.115778.
[3] M.F. Campbell, T.J. Celenza, F. Schmitt, J.W. Schwede, I. Bargatin, Progress toward high power output in thermionic energy converters, Adv. Sci. 8 (2021), 2003812, https://doi.org/10.1002/advs.202003812.
[4] A. Datas, Hybrid thermionic-photovoltaic converter, Appl. Phys. Lett. 108 (2016) 1203–1232, https://doi.org/10.1063/1.4945712.
[5] A. Datas, R. Vaillon, Thermionic-enhanced near-field thermophotovoltaics, Nano Energy 61 (2019) 10–17, https://doi.org/10.1016/j.nanoen.2019.04.039.
[6] A. Bellucci, M. Mastellone, V. Serpente, M. Girolami, S. Kaciulis, A. Mezzi, D. M. Trucchi, E. Antolín, J. Villa, P.G. Linares, A. Martí, A. Datas, Photovoltaic anodes for enhanced thermionic energy conversion, ACS Energy Lett. 5 (2020) 1364–1370, https://doi.org/10.1021/acsenergylett.0c00022.
[7] A. Bellucci, P. García-Linares, A. Martí, D.M. Trucchi, A. Datas, A three-terminal hybrid thermionic-photovoltaic energy converter, Adv. Energy Mater. (2022), 2200357, https://doi.org/10.1002/aenm.202200357.
[8] D.M. Trucchi, A. Bellucci, M. Girolami, P. Calvani, E. Cappelli, S. Orlando, R. Polini, L. Silvestroni, D. Sciti, A. Kribus, Solar thermionic-thermoelectric generator (ST2G): concept, materials engineering, and prototype demonstration, Adv. Energy Mater. 8 (2018), 1802310, https://doi.org/10.1002/aenm.201802310.
[9] H. Naito, Y. Kohsaka, D. Cooke, H. Arashi, Development of a solar receiver for a high-efficiency thermionic/thermoelectric conversion system, Sol. Energy 58 (1996) 191–195, https://doi.org/10.1016/S0038-092X(96)00084-9.
[10] J.W. Schwede, T. Sarmiento, V.K. Narasimhan, S.J. Rosenthal, D.C. Riley, F. Schmitt, I. Bargatin, K. Sahasrabuddhe, R.T. Howe, J.S. Harris, N.A. Melosh, Z. X. Shen, Photon-enhanced thermionic emission from heterostructures with low interface recombination, Nat. Commun. 4 (2013) 1576, https://doi.org/10.1038/ncomms2577.
[11] J.W. Schwede, B. Igor, D.C. Riley, B.E. Hardin, S.J. Rosenthal, S. Yun, S. Felix, P. Piero, R.T. Howe, S. Zhi-Xun, Photon-enhanced thermionic emission for solar concentrator systems, Nat. Mater. 9 (2010) 762–767, https://doi.org/10.1038/nmat2814.
[12] E. Rahman, A. Nojeh, Semiconductor thermionics for next generation solar cells: photon enhanced or pure thermionic? Nat. Commun. 12 (2021) 4622, https://doi.org/10.1038/s41467-021-24891-2.
[13] G. Segev, Y. Rosenwaks, A. Kribus, Limit of efficiency for photon-enhanced thermionic emission vs. photovoltaic and thermal conversion, Sol. Energy Mater. Sol. Cells 140 (2015) 464–476, https://doi.org/10.1016/j.solmat.2015.05.001.
[14] G. Xiao, G. Zheng, D. Ni, Q. Li, M. Qiu, M. Ni, Thermodynamic assessment of solar photon-enhanced thermionic conversion, Appl. Energy 223 (2018) 134–145, https://doi.org/10.1016/j.apenergy.2018.04.044.
[15] A. Varpula, K. Tappura, M. Prunnila, Si, GaAs, and InP as cathode materials for photon-enhanced thermionic emission solar cells, Sol. Energy Mater. Sol. Cells 134 (2015) 351–358, https://doi.org/10.1016/j.solmat.2014.12.021.
[16] K. Wang, G. Wang, R. Fu, H. Tran, B. Chang, L. Yang, High-performance Photon-enhanced thermionic emission solar energy converters with AlxGa1−xAs/GaAs cathode under multilevel built-in electric field, Opt Commun. 402 (2017) 85–90, https://doi.org/10.1016/j.optcom.2017.05.030.
[17] C. Feng, Y. Zhang, Y. Qian, Z. Wang, J. Liu, B. Chang, F. Shi, G. Jiao, High-efficiency AlxGa1−xAs/GaAs cathode for photon-enhanced thermionic emission solar energy converters, Opt Commun. 413 (2018) 1–7, https://doi.org/10.1016/j.optcom.2017.12.027.
[18] L. Liu, Y. Diao, S. Xia, High-performance GaAs nanowire cathode for photon-enhanced thermionic emission solar converters, J. Mater. Sci. 54 (2019) 5605–5614, https://doi.org/10.1007/s10853-018-03231-8.
[19] A.N.M.T. Elahi, D. Jensen, M. Ghashami, K. Park, Comprehensive energy balance analysis of photon-enhanced thermionic power generation considering concentrated solar absorption distribution, Sol. Energy Mater. Sol. Cells 226 (2021), 111067, https://doi.org/10.1016/j.solmat.2021.111067.
[20] S. Su, Y. Wang, T. Liu, G. Su, J. Chen, Space charge effects on the maximum efficiency and parametric design of a photon-enhanced thermionic solar cell, Sol. Energy Mater. Sol. Cells 121 (2014) 137–143, https://doi.org/10.1016/j.solmat.2013.11.008.
[21] Y. Wang, H. Li, H. Hao, J. Chen, S. Su, Optimal design of the interelectrode space in a photon-enhanced thermionic emission solar cell, Appl. Therm. Eng. 157 (2019), 113758, https://doi.org/10.1016/j.applthermaleng.2019.113758.
[22] A. Datas, R. Vaillon, Thermionic-enhanced near-field thermophotovoltaics for medium-grade heat sources, Appl. Phys. Lett. 114 (2019), 133501, https://doi.org/10.1063/1.5078602.
[23] X. Liu, H. Xia, Y. Xuan, Effects of near-field photon tunneling on the performance of photon–enhanced thermionic emission energy conversion, J. Quant. Spectrosc. Radiat. Transfer 222–223 (2019) 223–228, https://doi.org/10.1016/j.jqsrt.2018.10.036.
[24] H. Qiu, K. Wang, P. Yu, M. Ni, G. Xiao, A third-order numerical model and transient characterization of a β-type Stirling engine, Energy 222 (2021), 119973, https://doi.org/10.1016/j.energy.2021.119973.
[25] G. Xiao, H. Qiu, K. Wang, J. Wang, Working mechanism and characteristics of gas parcels in the Stirling cycle, Energy 229 (2021), 120708, https://doi.org/10.1016/j.energy.2021.120708.
[26] G. Segev, Y. Rosenwaks, A. Kribus, Loss mechanisms and back surface field effect in photon enhanced thermionic emission converters, J. Appl. Phys. 114 (2013), 044505, https://doi.org/10.1063/1.4816256.
[27] M. Beaudoin, A.J.G. DeVries, S.R. Johnson, H. Laman, T. Tiedje, Optical absorption edge of semi-insulating GaAs and InP at high temperatures, Appl. Phys. Lett. 70 (1997) 3540–3542, https://doi.org/10.1063/1.119226.
[28] M. Sotoodeh, A.H. Khalid, A.A. Rezazadeh, Empirical low-field mobility model for III–V compounds applicable in device simulation codes, J. Appl. Phys. 87 (2000) 2890–2900, https://doi.org/10.1063/1.372274.
[29] R.J. Nelson, R.G. Sobers, Minority-carrier lifetimes and internal quantum efficiency of surface-free GaAs, J. Appl. Phys. 49 (1978) 6103–6108, https://doi.org/10.1063/1.324530.
[30] Y. Rosenwaks, L. Burstein, Y. Shapira, D. Huppert, Effects of reactive versus unreactive metals on the surface recombination velocity at CdS and CdSe(1120) interfaces, Appl. Phys. Lett. 57 (1990) 458–460, https://doi.org/10.1063/1.103665.
[31] A.D. Rakić, M.L. Majewski, Modeling the optical dielectric function of GaAs and AlAs: extension of Adachi's model, J. Appl. Phys. 80 (1996) 5909–5914, https://doi.org/10.1063/1.363586.
[32] H. Yuan, S. Chang, I. Bargatin, N.C. Wang, D.C. Riley, H. Wang, J.W. Schwede, J. Provine, E. Pop, Z.-X. Shen, P.A. Pianetta, N.A. Melosh, R.T. Howe, Engineering ultra-low work function of graphene, Nano Lett. 15 (2015) 6475–6480, https://doi.org/10.1021/acs.nanolett.5b01916.
[33] E. Rahman, A. Nojeh, Interplay between near-field radiative coupling and space-charge effects in a microgap thermionic energy converter under fixed heat input, Phys. Rev. Appl. 14 (2020), 024082, https://doi.org/10.1103/PhysRevApplied.14.024082.
[34] D. Jensen, A.N.M. Taufiq Elahi, M. Ghashami, K. Park, Submicrometer-gap thermionic power generation based on comprehensive modeling of charge and thermal transport, Phys. Rev. Appl. 15 (2021), 024062, https://doi.org/10.1103/PhysRevApplied.15.024062.
[35] L.G. Thieme, Low-power Baseline Test Results for the GPU 3 Stirling Engine, NASA-TM-79103, NASA Lewis Research Center, Cleveland, OH, USA, 1979.